Taylor-couette-poiseuille flow heat transfer in a high taylor number test rig

Phillip B. Swann[1,*], Hugh Russell[1], Ingo H. Jahn[1]

[1]The University of Queensland, Brisbane, QLD 4072, Australia

Abstract

As technology advances, rotating machinery are operating at higher rotational speeds and increased pressures with greater heat concentration (i.e. smaller and hotter). This combination of factors increases structural stresses, while increasing the risk of exceeding temperature limits of components. To reduce stresses and protect components, it is necessary to have accurately designed thermal management systems with well-understood heat transfer characteristics. Currently, available heat transfer correlations operating within high Taylor number (above 1×10^{10}) flow regimes are lacking. In this work, the design of a high Taylor number flow experimental test rig is presented. A non-invasive methodology, used to capture the instantaneous heat flux of the rotating body, is also presented. Capability of the test rig, in conjunction with the use of high-density fluids, increases the maximum Taylor number beyond that of previous works. Data of two experiments are presented. The first, using air, with an operating Taylor number of $8.8 \pm 0.8 \times 10^7$ and an effective Reynolds number of $4.2 \pm 0.5 \times 10^3$, corresponds to a measured heat transfer coefficient of $1.67 \pm 0.9 \times 10^2$ W/m^{2}K and Nusselt number of $5.4 \pm 1.5 \times 10^1$. The second, using supercritical carbon dioxide, demonstrates Taylor numbers achievable within the test rig of $1.32 \pm 0.8 \times 10^{12}$. A new correlation using air, with operating Taylor numbers between 7.4×10^6 and 8.9×10^8 is provided, comparing favourably with existing correlations within this operating range. A unique and systematic approach for evaluating the uncertainties is also presented, using the Monte-Carlo method.

Introduction

Rotating machinery is used in a wide variety of applications, from turbines and electric generators to motors and workshop equipment. Thermal management has been of increasing interest as machines become smaller and faster (Heshmat et al., 2018; Yin et al., 2018). High temperature gradients can cause large thermal stresses and shorten the life of temperature sensitive components such as seals, shafts, discs, and bearings. As well as minimizing thermal stresses, minimizing coolant flows is essential to the efficient operation of most rotating machinery. It is therefore critical to have accurate models of the cooling mechanisms present and knowledge of the heat transfer rates to prevent undue stresses and ensure coolant flow rates are minimized.

Convective heat transfer and fluid dynamics are intrinsically linked, and therefore it is necessary to have a good understanding of the effect of changing fluid flow regimes on heat transfer rates. Typically, rotating machines involve a shaft with a static outer casing and a small annulus filled with gas or oil for thermal management and lubrication purposes.

The fluid regime which occurs in this mechanical set-up is known as Taylor-Couette (T-C) flow. Adding a mass flow rate in the axial direction results in Taylor-Couette-Poiseuille (T-C-P) flow (Fénot et al., 2011). These flows are described using the Taylor (Equation 1) and axial Reynolds (Equation 2) numbers, defined as;

$$\text{Ta} = \frac{\rho^2 \omega^2 R_{\text{inner}} (D_h/2)^3}{\mu^2} \qquad (1)$$

$$\text{Re}_a = \frac{\rho V_a D_h}{\mu} \qquad (2)$$

The Taylor number is the ratio of centrifugal (rotational) forces to viscous forces, while the axial Reynolds number is the ratio of inertia (axial) forces to viscous forces. In both parameters, the characteristic length used is the hydraulic diameter of the annulus (defined as $2 \times c$ where c is the radial clearance). Nusselt number is often presented against an effective Reynolds number, defined in Equation 3, as this is thought to capture the coupling of axial and rotational components of the flow field for Taylor-Couette-Poiseuille regimes.

$$\text{Re}_{\text{eff}} = \frac{\rho \sqrt{V_\phi^2 + V_a^2} \, D_h}{\mu} \qquad (3)$$

These non-dimensional numbers describe the behaviour of fully developed T-C-P flow within the annulus. The work of Jakoby et al. (1998) investigate the effect of flow development on heat transfer rates and describe the effective Reynolds number using the axial length, L. It is put forward that the dominance of the axial flow on heat transfer before the boundary layers on the inner and outer wall have mixed, indicates that the heat transfer must be related to length as well as annulus height. The length dependent Nusselt number is defined in Equation 4, where $\overline{\text{Nu}}$ is the global Nusselt number calculated by integration of the local heat transfer coefficients.

$$\text{Nu} = \left(\frac{\overline{\text{Nu}}L}{2c} \right) \qquad (4)$$

Many researchers have investigated T-C and T-C-P flow heat transfer, resulting in several review papers (Childs and Long, 1996; Fénot et al., 2011; Howey et al., 2012; Dawood et al., 2015). Although there have been many experimental and numerical studies performed, heat transfer measurements in flows with Taylor numbers above 1×10^{10} are lacking.

As research into improving industry operations and equipment continues, high density, low viscosity fluids, such as supercritical carbon dioxide (Keep et al., 2017; Heshmat et al., 2018), become more prominent and desirable for efficient operation. As these new designs are operating within a higher Taylor number regime, extensions to existing heat transfer correlations, backed by new high-quality experimental data, are essential to produce robust and efficient thermal management systems.

This paper describes the design of a test rig and methodology for measuring T-C-P heat transfer rates in high Taylor number flows. The maximum design Taylor number for the rig, when operating with supercritical carbon dioxide (sCO$_2$) is 1×10^{12} (up to 1×10^9 with air). In the current work, raw data of two experiments are presented. First, an air experiment showing a maximum Taylor number of approximately 1.27×10^9. A second experiment is shown using sCO$_2$, achieving a maximum Taylor number of 1.42×10^{12}, demonstrating the high Taylor number capability of the rig. A series of air experiments has resulted in a Nusselt number correlation between Taylor numbers of 7.4×10^6 to 8.9×10^8. This new correlation is discussed and compared with existing literature within this Taylor number range, validating the test rig operation, and highlighting challenges associated with T-C-P flow heat transfer measurements.

The paper is structured as follows. First, a short review of previous experiments to characterise T-C-P flows is presented. This is followed by a description of the test rig design, including CFD simulations to show the flow structure within the test section. Then a description of the methodology detailing the calculation of the heat transfer coefficient and uncertainty quantification using the Monte-Carlo method is presented. Lastly, the two sets of data are analysed, and a new correlation for air is presented and compared with literature.

Literature review

Many researchers have performed experiments to determine both flow regime transitions (Smith and Townsend, 1982; Masuda et al., 2018) and heat transfer characteristics (Aoki et al., 1967; Ball et al., 1989) for T-C and T-C-P flow regimes. To date, the most extensive range of heat transfer data for T-C-P flows has been compiled by Fénot et al. (2011) spanning a range of $Ta = 0$ to 1.2×10^{11} and $Re_a = 2.93 \times 10^2$ to 1.37×10^6. In some industrial applications, supercritical carbon dioxide turbomachinery, for example, Taylor numbers greater than 1×10^{11} may be encountered. As T-C-P flows are inherently unsteady and three dimensional, using high fidelity CFD simulations (e.g. LES or DNS) are not tenable for obtaining the required amounts of data to produce high quality correlations. Hence, new experimental data are necessary at these flow conditions.

Experimental heat transfer data gathered for the highest Taylor number range (up to 1.2×10^{11}) is currently presented by Childs and Turner (1994). Their experimental set-up used a 0.4 m diameter rotor, rotated at speeds up to 10,000 RPM and an axial mass flow rate of 4 kg.s^{-1}. This arrangement gave Taylor numbers between 0 to 1.2×10^{11}, due to the rotor's high surface speeds. A large ducted fan system was used to draw air at atmospheric conditions through an initial non-rotating zone, used to ensure fully developed flow at the test region Childs and Turner (1994).

The large diameter rotor used by Childs and Turner (1994) prevented the use of significant pressures and higher density fluids. Higher pressures at these diameters would require a prohibitively thick outer casing to ensure safe operation. The design also did not allow for alternate fluids at varying conditions to be used, limiting the range of fluid properties available.

A critical aspect of establishing accurate correlations is the heat transfer measurement to the rotating shaft. Childs and Turner (1994) used embedded heat transfer gauges, however, this can limit the available test conditions due to the sensor and necessary equipment operating limits. A more extensive study of measurement techniques was performed by Seghir-Ouali et al. (2006) who determined the convective heat transfer coefficient for air passing through a rotating cylinder, known as Hagen-Poiseuille flow. Their setup consisted of power regulated infrared heaters to heat the test section and an infrared camera to measure the temperature history of the shaft surface. The team determined the convective heat transfer using three different methods; a steady state inverse discretized model, a thermally thin wall assumption method, and an analytical method (Seghir-Ouali et al., 2006). All three methods were found to be of similar relative uncertainty in the final heat transfer coefficient calculation. Key advantages of the heat transfer measurement techniques employed by Seghir-Quali et al. (2006) are that they are non-invasive, allowing instrumentation to be kept outside of the test rig, removing constraints on the achievable conditions.

A further evolution of heat transfer measurement techniques, is the use of system inversion for transient temperature measurements as presented by Battaglia et al. (2001). This method is an extension to that presented by Schultz and Jones (1973) used extensively in hypersonic wind tunnel testing, allowing for the removal of the semi-infinite assumption. The method presented assumes that the thermal system is linear and thus temperature response is the convolution of the heat flux with the impulse response of the system in question. Thus, by identifying the system response and de-convolving the temperature history, the transient input of heat flux can be recovered. This process was applied by Battaglia et al. (2001) to determine the heat flux between a cutting tool and material. The identified system was used to estimate both temperature and heat flux on the cutting surface. It was found that the calculated temperature profile from the convolution was "very close" to the experimentally measured temperature. Another study was performed on null point calorimeters in high speed plasma flow characterization using the same method (Gardarein et al., 2009). It was found that the method performed better than other established experimental approaches.

One of the key advantages of this approach is that it does not assume a heat input function (e.g. step function) and thus, does not require a known temperature profile. It calculates an instantaneous heat input at each time interval. The method also does not require any knowledge of the fluid properties or flow regime to determine heat transfer rate. A variation of this method is used in this body of work.

Test rig

A picture of the test rig is shown in Figure 1, with a schematic representation displayed in Figure 2. The rig operates transiently whereby it is initially heated. Then, flow is initiated to cool the test section. With this approach, the initial temperature of the test rig is uniform and can be measured. Due to data being collected in the transient phase, before the effects of cooling are propagated to the outside of the casing, the outer thermal boundary conditions are simplified for the heat transfer analysis.
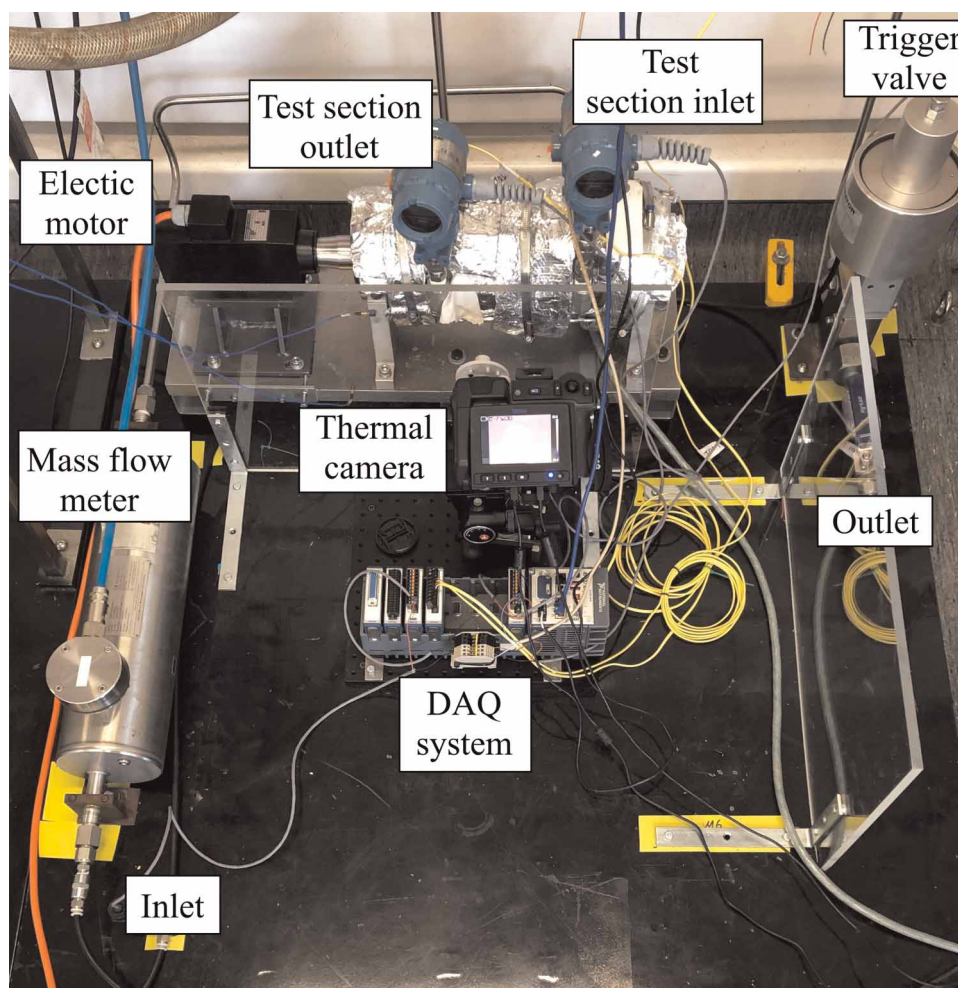
Figure 1. Photo of test rig.

The test section consists of an inlet and outlet plenum with a long annular section between them. The test section is designed to be long enough for flow to be fully developed before the flow reaches the optical windows, which is verified in the Simulation of Test Section part of the paper. A cross-section of the test section is also shown in Figure 2.

The test rig has a 10 MPa and 150°C operating pressure and temperature limit, providing the ability to test high density fluids. An electric motor is used to spin the shaft up to a maximum of 30,000 RPM. Combining this speed and utilising high density, low viscosity fluids such as sCO_2, Taylor numbers of 1.42×10^{12} and axial Reynolds numbers of 3.3×10^5 can be achieved. The mass flow rate through the test section can be varied from 0.0015 to 0.004 kg/s for air and 0.015 to 0.024 kg/s for sCO_2 by the orifice plates placed at the outlet. These design aspects provide critical control over the rotational and axial components of fluid flow making a range of test conditions possible. The key parameters are summarised in Table 1.

To avoid the need for seals, the shaft is connected to a Perske VS31.09 electric motor via a magnetic coupling manufactured by DST Magnetic Couplings, allowing the shaft and bearings to be immersed in the working fluid. The pressure vessel (and shaft) are heated using 4 m of 50PHT Heat Trace cable connected to an RS PRO 48×48 temperature controller unit. The controller thermocouple is placed on the outside of the casing, shown in Figure 2.

Test procedure

The operating procedure of the test rig is provided in Table 2. The first step is to bring the test section to temperature while the shaft is stationary, and the test section is at low pressure. Once the shaft and casing have reached uniform and steady temperature, the upstream isolation valve is opened, and the test section is pressurised. Once the introduced gas has reached temperature and the temperature of all components in the test section have equilibrated, tests commence. During a test, the shaft is first brought to speed. Once the desired speed has been reached, the trigger valve (located at the outlet as shown in Figure 2) is opened. This allows the
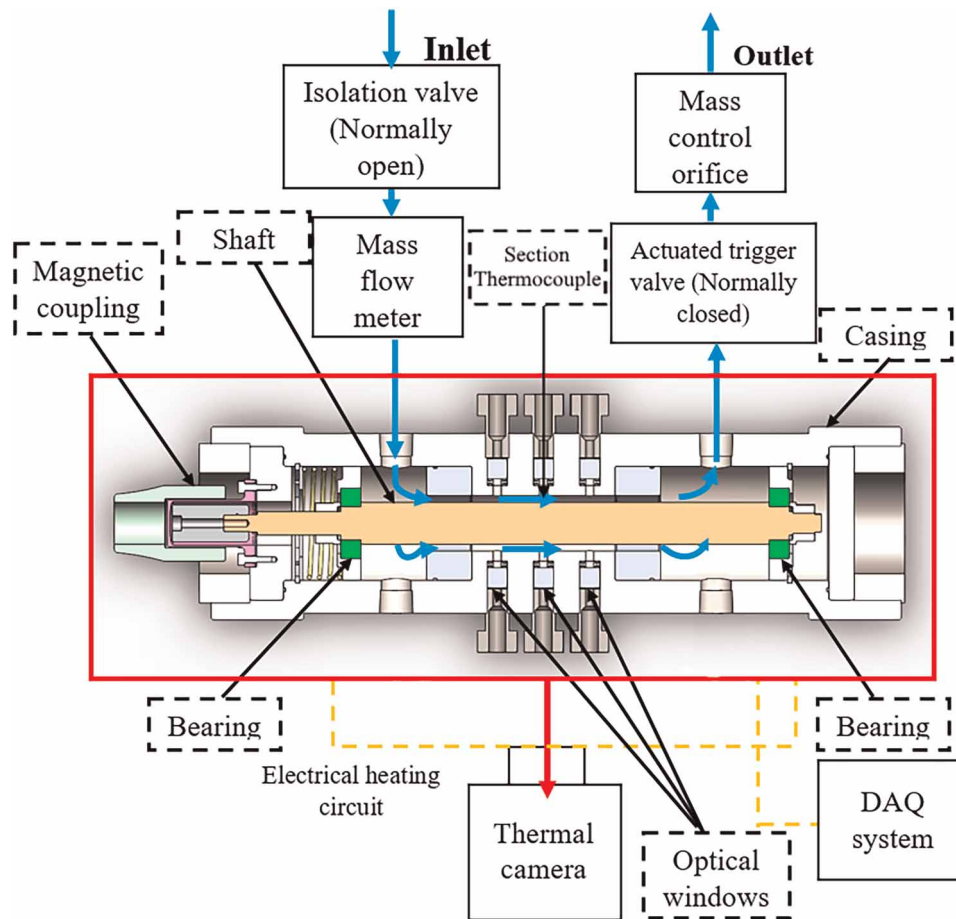
Figure 2. Test rig schematic.

hot gas within the rig to escape and a cold slug of gas, originally upstream of the mass flow meter, to flow through the test rig. The test-time starts when this cold slug reaches the inlet plenum of the test section. Each test ends by closing the trigger valve. During tests, the mass flow rate and pressure inside the rig are controlled by the orifice plate positioned at the downstream end of the test section. The temperature is controlled by the heat transfer characteristics of the operating parameters of that test.

The transient nature of the tests, and the cold gas slug arriving in the hot test section, allows an analytical inverse deconvolution technique to be used in determining the convective heat transfer from the shaft surface temperature history. Shaft surface temperature is measured using a thermal camera, described in detail in later sections.

Sensors and data acquisition

The inlet and outlet plenums of the test section include Rosemount 2051 pressure transmitters and K-type thermocouples. A third thermocouple is positioned radially in the centre of the annular flow, and axially at the position of the surface temperature measurement, located 180° to the optical windows. This is used to provide the fluid reference temperature, T_f. For tests with air, the downstream orifice plate is used to calculate mass flow rate through the rig. When using air, Annex A of the International Standard ISO 5167 is used to evaluate the mass flow rate through the orifice plate. The outlet plenum measurements are used as the upstream conditions, with atmospheric conditions for the downstream. For operating with higher density fluids, such as sCO_2, the Siemens SITRANS FC MASS 2100-DI15 Coriolis type mass flow meter is available. The pressure, temperature, and mass flow rate measurements are routed through a Compact-RIO NI 9072 chassis and a bespoke LabVIEW data acquisition program, with data sampled at 200 Hz. This sample rate is sufficient to capture the change in pressure as the cold gas slug passes into the test section.

The accuracy of the K-type thermocouples, Rosemount pressure transmitters and Coriolis mass flow meter are ±2.2 K, ±0.026 MPa and ±0.15%, respectively. These uncertainties were provided by the manufacturer of the sensors. However, thermocouple and pressure transmitter calibrations were also conducted. A 95% confidence interval in the calibrations over the range of temperatures and pressures of testing were found to be ±3.6 K and

Table 1. Test rig design parameters.

Parameter	Maximum (or Nominal)	Minimum
Shaft diameter (mm)	25	–
Annulus height (mm)	4	–
Test section length (mm)	136	–
Shaft speed (RPM)	30,000	0
Shaft Initial Temperature (°C)	150	50
Test Duration	15–60	–
Air		
Fluid Temperature (°C)	ambient	–
Fluid Pressure (MPa)	0.25	≥ambient
Mass flow rate (kg/s)	0.004	0.0015
Taylor number	1×10^9	0
Axial Reynolds number	4.6×10^3	1.7×10^3
CO_2		
Fluid Temperature (°C)	150	30
Fluid Pressure (MPa)	10	0.25
Mass flow rate (kg/s)	0.024	0.015
Taylor number	1×10^{12}	0
Axial Reynolds number	3.3×10^5	1.1×10^4

Table 2. Test rig operating procedure (see Figure 2 for reference).

Step	Description	Test Section State
1	Heat up test section	Heated
2	Open isolation valve	Heated, Pressurised
3	**Begin Test** – Bring shaft to speed	Heated, Pressurised, Spinning
4	Open trigger valve	Heated, Pressurised, Spinning, Gas flowing
5	*Test time*	As above
6	Close trigger valve	Heated, Pressurised, Spinning
7	**End Test** – Stop Shaft	Heated, Pressurised

±0.026 MPa, respectively. The larger of the uncertainties in each sensor is used in the uncertainty quantification section.

Aremco 840 M high emissivity paint with an emissivity of 0.95 ± 0.05 is used on the shaft surface for a high infrared signal to be received by the FLIR T650sc thermal imaging camera. The thermal camera is routed directly to a PC and is operated using the FLIR ResearchIR MAX software. The data collected using the software is amalgamated and analysed using a bespoke Python script.

Simulation of test section

To better understand the flow behaviours within the test section, to confirm that end-effects are negligible, and to show that flow structures expected from T-C-P flow are established in the test region, a 3D Computational Fluid Dynamics (CFD) analysis was performed. Understanding these aspects has assisted in interpreting the heat transfer data gathered.

Simulation setup

The ANSYS CFX CFD solver was used to perform the analysis. A schematic of the simulation domain is displayed in Figure 3, showing where the domain boundaries are defined. A mass flow rate inlet was defined on the face of the tube stub section, located at the entrance to the inlet plenum. A pressure outlet was defined at the outlet plenum in a similar manner. A rotating, constant temperature wall was defined for the inner boundary of the fluid domain (shaft surface). The outer boundary was set to a stationary wall at constant temperature (inner casing surface). The height of the first radial cell was set to 3.5×10^{-6} m at both walls, resulting in a y+ value of 0.6, using air as the domain fluid meaning the boundary layer and viscous sub-layer have been fully resolved. All simulations were performed with air to reduce the total number of cells required near the wall.

The momentum equations were closed with the k-ω SST turbulence model. As the flow is incompressible ($M < 0.3$), the equations were solved using the SIMPLE algorithm, including the energy equation to account for temperature and density variations. Boundary condition values are displayed in Table 3.

Verification

Due to the three-dimensional, unsteady nature of T-C-P flow and its strong coupling with heat transfer, a study was conducted to determine the suitability of steady-state simulations to accurately represent the flow field within the test rig.
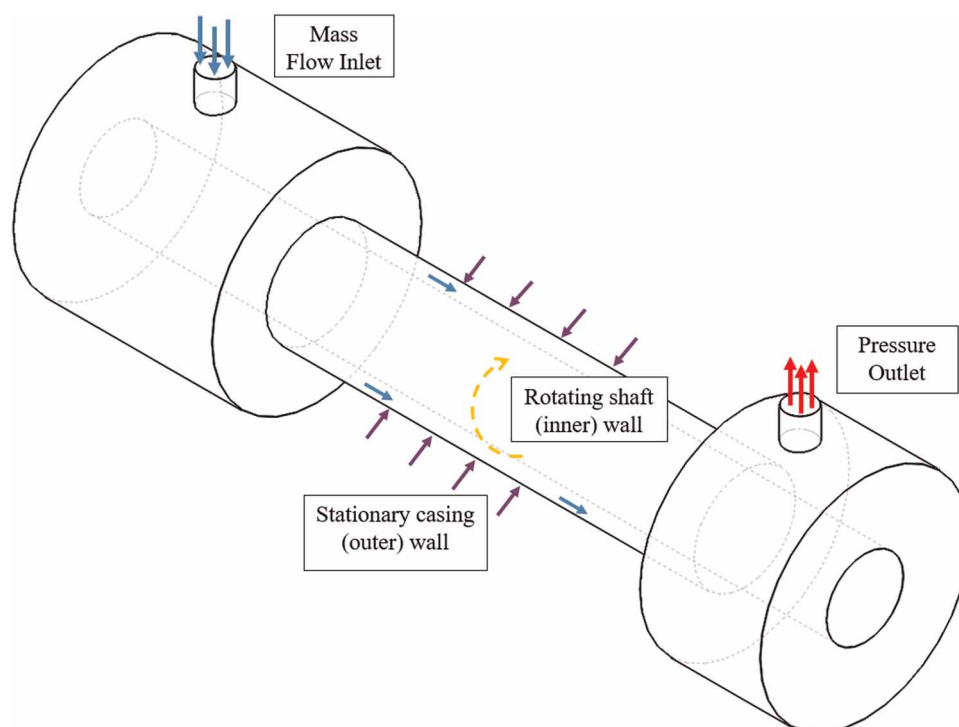

Figure 3. CFD boundary condition setup.

Table 3. CFD study boundary conditions.

Boundary	Type	Value
Inlet	Mass flow	0.004 kg/s
	Temperature	40°C
Outlet	Pressure	0.28 MPa
Shaft wall	Moving wall	20,000 RPM
	Temperature	75°C
Casing wall	Stationary wall	N/A
	Temperature	90°C

To simplify the flow field, the comparison is based on a Taylor-Couette flow scenario (no axial flow). For this, the inlet boundary was changed to a fixed pressure, at 0.28 MPa and outlet boundary was replaced by a stationary wall with temperature, 90degC. The remaining conditions for both steady and unsteady RANS simulations were taken from Table 3.

Figure 4 shows the invariant q criterion iso-surface for the transient (bottom) and steady (top) simulations. From the figure, in both cases, vortex cell structures are formed within the test section length. The transient case shows clear vortex centres. The steady state case shows mixed or smeared vortex centres, which is due to the
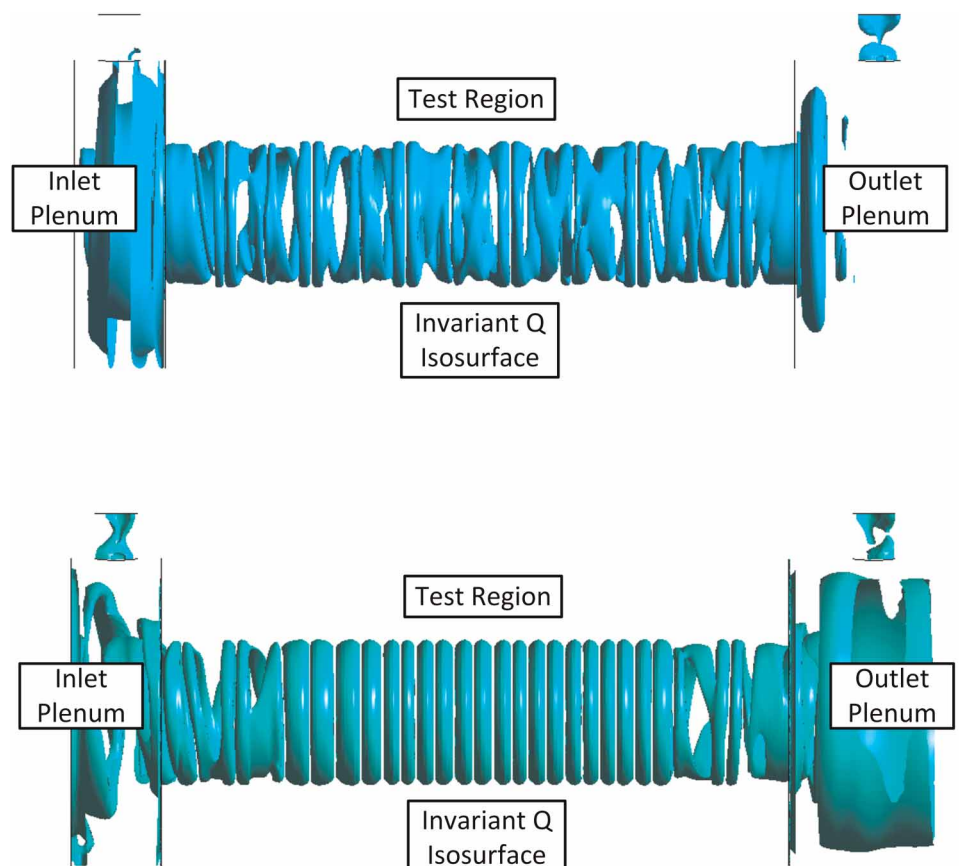

Figure 4. Invariant Q isosurface for unsteady (bottom) and steady (top) case, indicating vortex centres.
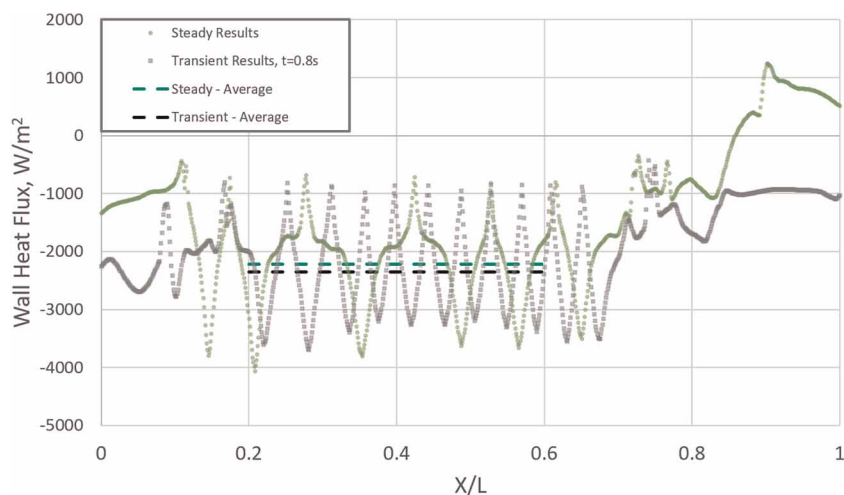
Figure 5. Steady and unsteady heat flux along shaft (inner) wall.

averaging nature of the steady solution of an unsteady phenomenon. By prescribing fixed temperatures on the inner and outer wall, steady simulations provide an averaged snap-shot of the flow.

The differences in resulting flow structures, however, does not appear to significantly impact the average heat transfer rate over the test section as shown in Figure 5. This figure shows the shaft (inner) wall heat flux, circumferentially averaged around four equidistant lines. The transient results are taken at 0.8 s from the simulation start, at which point the spatially averaged shaft surface heat flux had reached a "steady" value along the shaft surface. Looking at the average of the two cases, similar heat fluxes of -2.22×10^3 W/m^2 for the steady case and -2.36×10^3 W/m^2 for the unsteady case were observed, giving an error of 6.3%.

As the steady simulation resolves all flow structures and, more importantly, the resulting heat transfer behaviours of interest, steady simulations were used to generate all subsequent simulation data presented.

A mesh independence study was performed for the steady simulations. Figure 6 shows the heat transfer coefficient (HTC) for the centre of the test region sufficiently far from the shaft ends to eliminate end effects, for three increasing mesh refinements. The HTC is calculated using the inner wall heat flux and difference between the inner and outer wall temperature. The average is also displayed. As the axial placement of the vortices shifts between the simulation runs, the raw HTC values for Ref #2 has been shifted axially to better illustrate agreement between T-C flow structures and corresponding HTC profiles.

This study shows a converging average HTC for increasing mesh refinements as also reported in Table 4. For the two finer meshes, 6.2×10^6 and 8.7×10^6 cells, the relative error in average HTC has reduced to 1.8%, sufficient for the current CFD analysis. These HTC results were also compared to literature for the relevant operating Taylor number (Ta $= 1.3 \times 10^8$). Using the correlation developed by Tachibana et al. (1960), the calculated
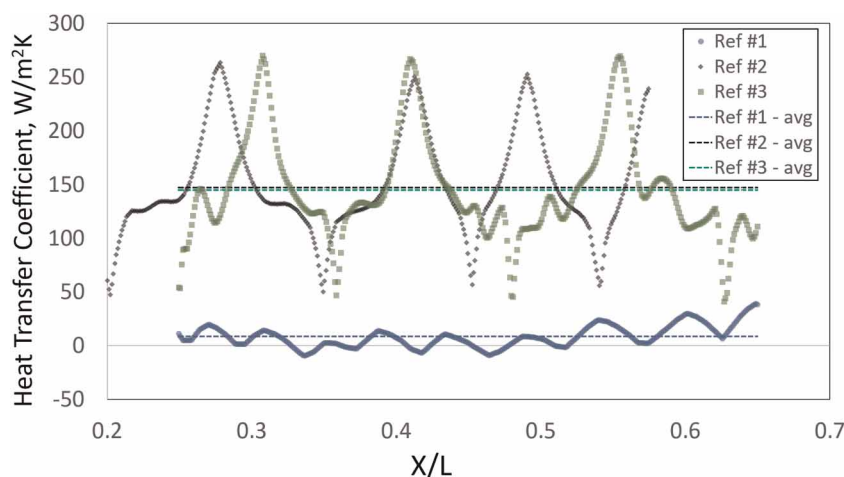

Figure 6. Steady state CFD mesh refinement study using heat transfer coefficient.

Table 4. CFD mesh refinement results.

Parameter	Ref #1	Ref #2	Ref #3
Cells	4.98×10^6	6.22×10^6	8.70×10^6
Average HTC (W/m^2 K)	8.45	147.3	144.7
% Error relative Ref #3	94.1	1.8	n/a

HTC value at simulation conditions was 142 W/m^{2}K. Using Ref #2 and Ref #3 the obtained values are within 3.7% and 1.9% of the literature correlation value, giving confidence to the simulation accuracy.

CFD results

To provide insight into the operation of the rig, T-C-P flow with boundary conditions prescribed in Table 3 was simulated. Figure 7 shows the corresponding results with temperature contours on the bottom half and velocity vectors on the top half. From these results, clear Taylor vortices and the corresponding localised enhancement in heat transfer by transport of hot fluid to the shaft, are evident within the test region. The test region was identi-fied by the presence of a regular helical flow structures and where heat transfer rate no longer increased with length.

Figure 8 displays the corresponding HTC profile along the shaft surface. HTC was calculated along four lines spanning the length of the test section and placed at 90-degree intervals around the inner wall of the flow domain and then circumferentially averaged. In this way, the inner wall heat flux and the difference between the inner wall temperature and temperature at the centre of the annulus were extracted. To minimise noise in the cal-culated HTC value and to remove entry length effects, the centre annulus temperatures were extracted using a linear regression fit along the test region only, with the "Development length" disregarded.

Figure 8 shows decreasing HTC up to $X/L = 0.4$. There is a significant fluctuation in HTC between $X/L = 0.4$ and 0.6, caused by the temperature difference between the centre of the annulus and shaft surface
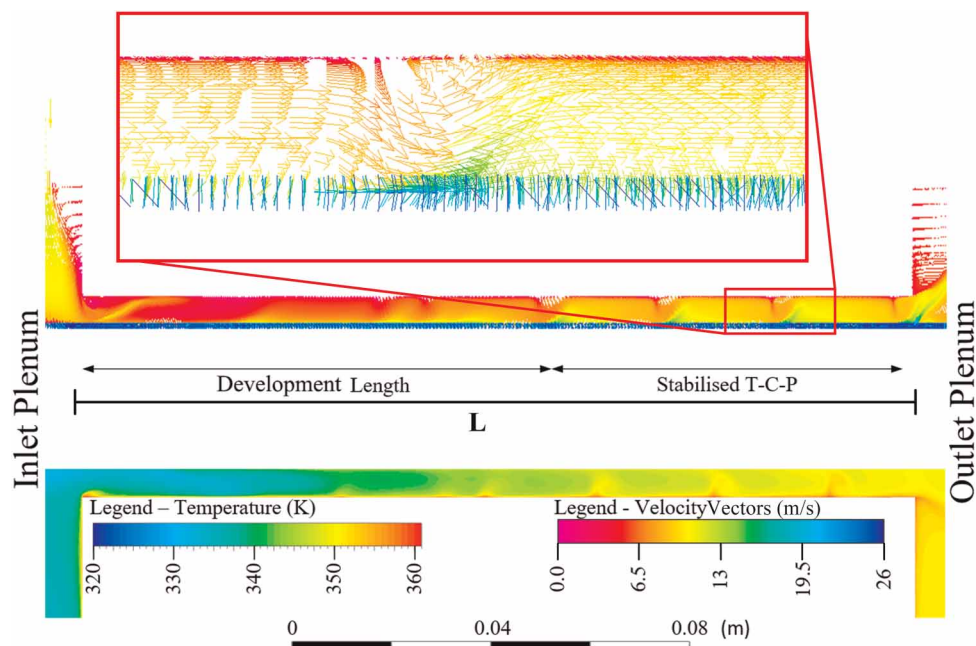

Figure 7. CFD results showing velocity vectors (top half of flow domain) and temperature contour (bottom half of flow domain). Development length and Stabilised T-C-P flow region are indicated. Inlet and outlet tube sections removed for clarity.
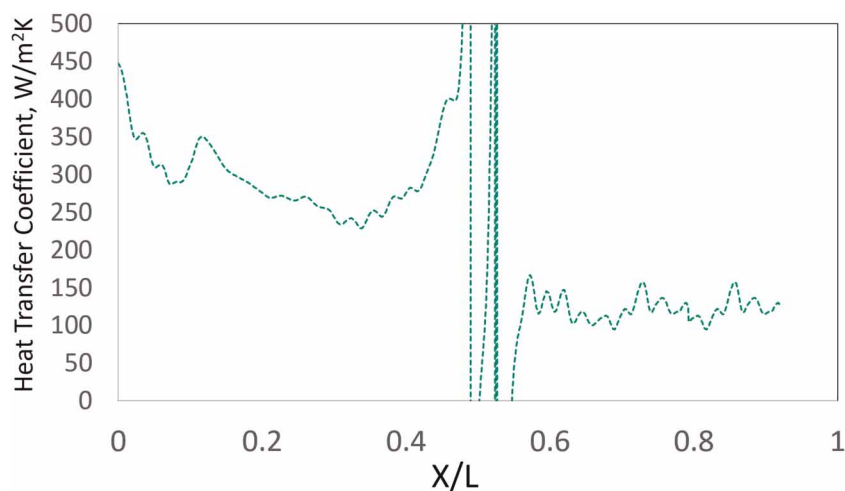
Figure 8. CFD HTC results showing stable HTC at stabilised flow position.

approaching zero. After $X/L = 0.6$, the HTC value stabilises. The stabilization of HTC matches the region of established Taylor vortices.

These simulations confirm that Taylor vortices form inside the test rig anulus and that by the measurement location used for the experiments, positioned at $X/L = 0.65$ from the test region start, stabilised T-C-P flow exists. The simulation conditions from Table 3 correspond to the highest axial flow velocity of the experimental cases, giving a conservative estimate of the development length.

Methodology

This section describes the necessary steps to determine the Heat Transfer Coefficient (HTC) from the measurements taken in the test rig. The determination of the HTC is a three-stage process. Each stage is described in the subsequent sections.

Measurement of surface temperature

The measurement of the shaft surface temperature is a two-stage process. First, the FLIR T650sc thermal camera is used to measure the thermal signal coming from the shaft surface. This produces the raw camera signal as counts. Second, the camera counts measurements are converted into temperature measurements via a two-point calibration curve, to account for losses in the light path, that is established before each series of tests and verified afterwards. This in-situ calibration accounts for the presence of lenses, optical windows, and the gas path between the window and shaft. A series of off-line experiments, covered in Swann (2020), were performed to determine that these have a consistent impact on camera signal and that their influences can be removed through the two-point calibration process.

As the test rig does not include instrumentation for direct measurement of the shaft surface temperature, T_s, it must be estimated from other thermocouples in the rig to allow for accurate calibration. A series of off-line calibration experiments were conducted that included an invasive thermocouple attached directly to the shaft. From these, it was established that the shaft surface temperature, T_s, used in the calibration process could be accurately estimated from the fluid reference temperatures taken in the inlet and outer plenums. The uncertainty associated with the approach is included as a calibration uncertainty in the later error propagation study.

Calculation of surface heat flux

From an energy balance point of view, the total heat transfer between the rotating shaft and cooling fluid comprises of conduction, convection, and radiation components. Due to the low temperature of the rig, the radiation component is sufficiently small so that it can be ignored without loss of accuracy. The conduction and convection components manifest as heat transfer from shaft to fluid, which is balanced by conduction within the shaft.

Previous works have shown that the temperature of a linear system can be represented as the convolution of the heat input to the system and the systems impulse response (Battaglia et al., 2001). Converting the analytical

equations for the shaft and fluid heat transfer into discrete form yields the following linear relationship between discrete heat flux and temperature values.

$$T = IQ = \begin{bmatrix} T_0 \\ T_1 \\ \vdots \\ T_N \end{bmatrix} = \begin{bmatrix} I_0 & 0 & \cdots & 0 \\ I_1 & I_0 & 0 & \vdots \\ \vdots & \vdots & \ddots & 0 \\ I_N & I_{N-1} & \cdots & I_0 \end{bmatrix} \begin{bmatrix} q_0 \\ q_1 \\ \vdots \\ q_N \end{bmatrix} \tag{5}$$

Therefore, taking the discrete measured temperature history, T_0 to T_N, and applying the system impulse response, I_0 to I_N, derived analytically, the corresponding discrete time history of the heat flux, q_0 to q_N, can be determined by taking the inverse of the impulse response matrix.

$$Q = I^{-1}T \tag{6}$$

To apply this method, firstly, it is necessary to define the governing equation for transient conduction heat transfer with relevant boundary and initial conditions. As the shaft has a high rotational speed, it can be assumed that any circumferential variations in heat transfer as experienced by the shaft surface are smeared out, and the circumferential component of the conduction equation inside the shaft is sufficiently small to be neglected. The axial component can also be neglected as the shaft starts off at a uniform temperature, and heat transfer only varies slowly in the axial direction along the test region, which means that during the initial transient phase, shaft temperatures are dominated by heat transfer in the radial direction.

From these assumptions, the governing equation is the 1-D (radial component) transient conduction heat equation in cylindrical coordinates shown in Equation 7. Corresponding boundary conditions and initial conditions are listed in Equations 8–10.

$$\frac{1}{\alpha}\frac{dT}{dt} = \frac{1}{r}\frac{d}{dr}\left(r\frac{dT}{dr}\right) \tag{7}$$

$$-k\frac{dT}{dr}\bigg|_{r=0} = 0 \tag{8}$$

$$-k\frac{dT}{dr}\bigg|_{r=R} = -q \tag{9}$$

$$T(r, 0) = 0 \tag{10}$$

Solving the governing equation using an auxiliary function and a separation of variables approach, leads to the temperature equation for a step response to input heat flux with magnitude q:

$$T(r, t) = q\left(\frac{r^2}{2kR} + \frac{2\alpha t}{kR}\right) + \sum_{n=0}^{\infty} C_n J_0(\lambda_n r)e^{-\lambda_n^2 \alpha t} \tag{11}$$

$$C_n = \frac{\int_0^R r(T_{\text{init}} - (qr^2/2kR))J_0(\lambda_n r)dr}{\int_0^R rJ_0(\lambda_n r)^2 dr} \tag{12}$$

$$J_1(\lambda R) = 0 \tag{13}$$

where J_0 and J_1 are the Zeroth and First Order Bessel functions of the first kind, respectively. Looking at Equations 11 and 12, the functions are linear with respect to the heat flux for the case that initial temperature, $T_{\text{init}} = 0$. This can be achieved by offsetting the discrete measured temperature series with the temperature at time, $t = 0$. The linearity is a necessary characteristic of the system to use the convolution of heat input and impulse response. The impulse response of the system is found by taking the derivative of the analytical temperature equation (Equation 14).

$$\frac{dT(r, t)}{dt} = q\left(\frac{2\alpha}{kR}\right) - \sum_{n=0}^{\infty} \lambda_n^2 \alpha C_n J_0(\lambda_n r)e^{-\lambda_n^2 \alpha t} \tag{14}$$

The impulse matrix is formulated using the time resolution of the temperature measurements. Using the impulse matrix and the temperature history obtained from the thermal camera measurements, the discrete heat flux vector can be determined through elementary matrix operations as defined in Equation 6.

Calculate HTC

From the heat flux vector, the heat transfer coefficient (HTC) is determined through Newton's law of cooling for all time intervals.

$$h_i = \frac{q_i}{(T_{si} - T_{fi})} \tag{15}$$

This equation uses the measured fluid temperature, T_f, and shaft surface temperature, T_s, as measured by the thermal camera and in-situ calibration. h_i is the instantaneous heat transfer coefficient (HTC) at time interval i. The temperature of the fluid at time interval i (T_{fi}) is determined by one of two ways. First, if the middle thermocouple positioned at the surface measurement location is present for a test, this measurement is used directly as T_{fi}. If this thermocouple was not present for the test, it is estimated by assuming a linear temperature profile between the inlet and outlet plenums to calculate the fluid temperature at the measurement location, $(0.5(T_{in} + T_{out}) + T_s)$. This method is used in the test displayed in Figure 9.

To determine the HTC for a given test, the cumulative average and variance of the HTC values is calculated. By inspection of the resulting curve, the region over which the HTC has stabilised is chosen. The final HTC value is then evaluated by averaging the raw HTC values over the chosen time interval. Further description of this process is provided in previous publications (Swann, 2020).

Uncertainty quantification

The detailed analysis of the uncertainty propagation and corresponding quantification is split into three steps: (1) Establish uncertainty in shaft surface temperature, (2) establish uncertainty in surface heat flux q, and (3) establish uncertainty in the HTC.

Shaft surface temperature uncertainty

Shaft surface temperature is measured using a calibrated IR camera. The calibration is performed using a linear curve-fit relating the raw camera counts to surface temperature. This calibration process accounts for the as-built optical losses and is performed against a K-type reference thermocouple (used to infer shaft temperature during calibration). The calibration curve is then offset to account for the difference in shaft and fluid temperature at the time of the daily calibration. This optical temperature measurement approach introduces a systematic uncertainty of ±4.9 K. In addition, there is a random uncertainty of ±0.3 K, inherent to the camera sensor.

Surface heat flux uncertainty

Surface heat flux, q_0 to q_N, is calculated using Equation 6, which is reliant on a series of discrete temperatures, T_0 to T_N. To propagate uncertainties through this process and to capture the impact of shaft properties and geometry, the Monte Carlo method is applied. For this, 900 discrete temperature series are created by varying the systematic and random uncertainty applied to inputs. First the same normally distributed systematic uncertainty is added across a temperature series, then normally distributed random uncertainties are added to each data point in that series. The 900 temperature series are created in this manner. This approach ensures consistent systematic errors are used for each discrete temperature series. For each temperature trace, the shaft geometry and properties are randomly selected based on square or normal distributions as displayed in Table 5.

An instantaneous heat flux series is calculated for each of the 900 discrete temperature series. The uncertainty in heat flux, q, is then established by taking the 95% confidence interval at each point in time.

To determine if 900 temperature traces is sufficient to capture the uncertainty limits, results from the Monte-Carlo analysis using 800 and 900 temperature traces were compared, giving a 95% confidence interval of $\pm 1.095 \times 10^2$ W/m^2 and $\pm 1.098 \times 10^2$ W/m^2, respectively. The difference in uncertainty is approximately 0.2%, demonstrating that the uncertainty limits are captured.
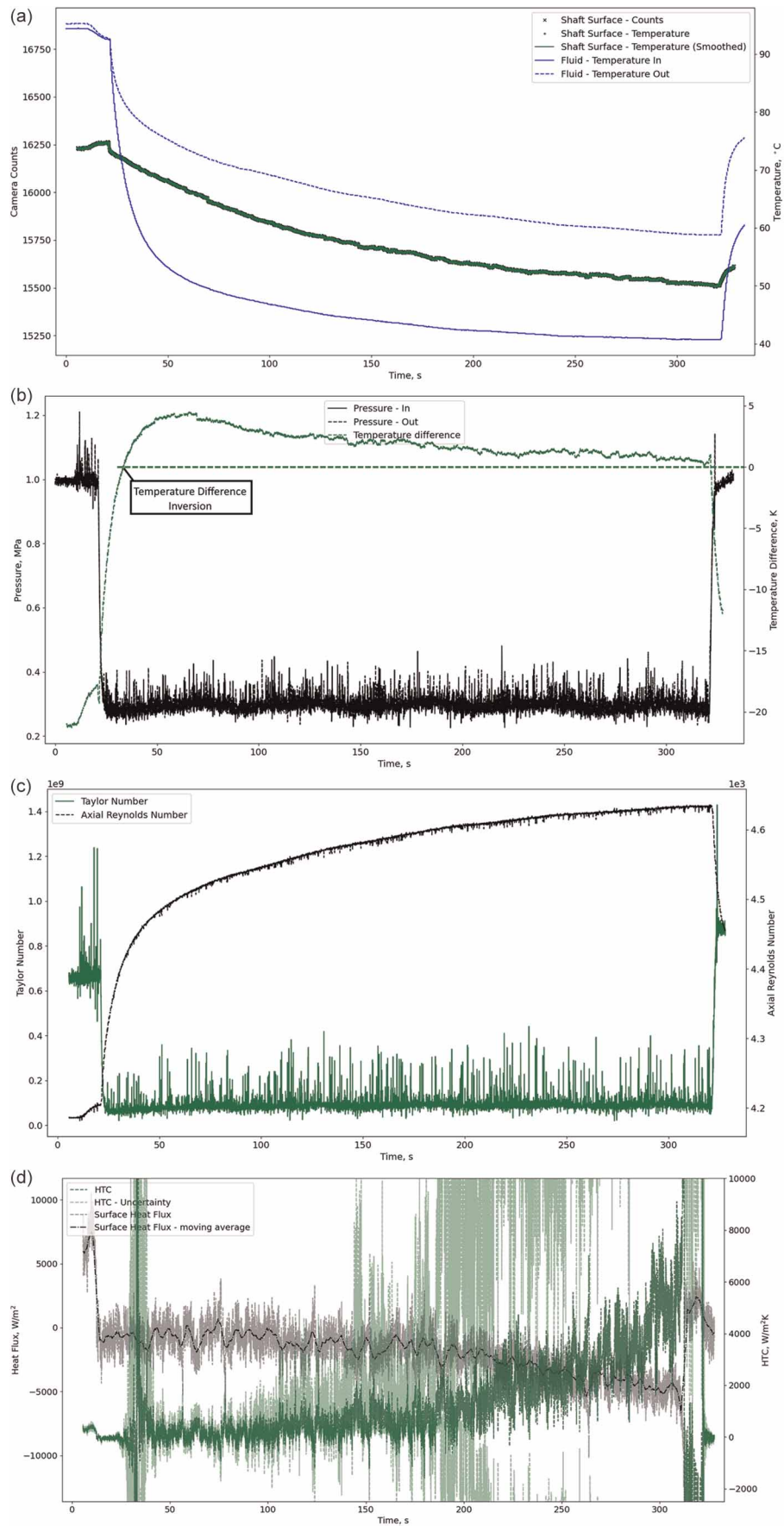
Figure 9. Air Test Results from top to bottom; (a) temperatures (b) pressure with shaft and fluid temperature difference (c) Taylor and axial Reynolds number (d) heat flux and HTC.

Table 5. Shaft property uncertainties.

Property	Uncertainty ($\pm$)	Distribution
Radius (m)	0.00025	square
Density (kg/m^3)	80	normal
Heat capacity (J/kg K^{-1})	50	normal
Conductive heat transfer coefficient (W/mK^{-1})	1.6	normal

HTC Uncertainty

The heat transfer coefficient (HTC) uncertainty is calculated using a further Monte Carlo simulation of Equation 15. In this equation, HTC is dependent on the heat flux, surface and fluid temperatures. The temperature measurements for the inlet and outlet plenums and middle thermocouple, used to calculate T_{fi} were calculated to be normally distributed. HTC is then calculated at each time interval for each series of heat flux and corresponding temperatures. The uncertainty in HTC is established by taking the 95% confidence interval of all the HTC traces over the time interval from which the final HTC value was determined.

Results and discussion

All raw data (sCO$_2$ and air) collected with the high Taylor number T-C-P flow heat transfer test rig can be found through the permanent University of Queensland repository (https://doi.org/10.14264/uql.2020.729).

Results with air

Results for a single test with nominal conditions in Table 6 are shown in Figure 9. Displayed in Figure 9a are the measured camera counts, the calculated shaft surface temperature, and air temperatures at the inlet and outlet plenums. Before the test begins, the shaft temperature is a constant at $T = 76°C$ followed by a short rise to $T = 77°C$ caused by the motor start. The test starts as the trigger valve is opened ($t = 20.6$ s) and the cooling air passes through the test section. Coincident with the pressure reduction, indicating flow, temperature begins to decrease ($t = 21.0$ s).

Table 6. Air test nominal settings.

Parameter	Value
Speed (RPM)	20,000
Fluid Inlet Temperature (°C)	40
Fluid Inlet Pressure (MPa)	1.0
Mass control orifice size (mm)	4.4
Test time (s)	300
Shaft Initial Temperature (°C)	90
Nominal Taylor Number	1×10^8
Nominal Axial Reynolds Number	4.2×10^3

Figure 9b shows the plenum pressures and difference in shaft surface and fluid temperatures. The region up to $t = 50$ s, shows a quickly changing temperature difference, where the cold gas slug enters the test section. The initial transient in temperature difference arises from the inflow of the cold air slug, pushing the temperature to approximately 5 K below that of the shaft temperature, inverting the heat transfer direction from heating to cooling. After this initial change, the difference between shaft and fluid temperature decreases from 4.9 to 1.2 K over the remaining test time.

Figure 9b also shows the pressure magnitudes of the inlet and outlet plenums. The pressure magnitudes across the test section are indiscernible. The motor is started just prior to the trigger valve opening, as prescribed in Table 2, coincident with a significant increase in measurement noise (increasing from ±0.03 MPa to ±0.3 MPa), observed at $t = 10.8$ s. A reduction in pressure, from 0.99 MPa to 0.28 MPa, at the start of the test ($t = 20.8$ s), indicating when air is venting through the orifice. After an initial start-up lasting approximately 4.1 s, pressure stabilises at 0.28 MPa.

Figure 9c shows the Taylor number and axial Reynolds number throughout the test time. The maximum Taylor number reached during the air test is approximately 1.27×10^9. The Taylor number magnitude shows a large drop, coincident with the drop in pressure, by a factor of 5. As density is linearly proportional to pressure and Taylor number is dependent on ρ^2 per Equation 1, pressure and Taylor number trends closely align. The average axial Reynolds number is approximately 4.2×10^3 across the test time. The axial Reynolds number is dominantly dependent on the mass flow rate ($\mathrm{Re}_{\mathrm{axial}} = \dot{m}c/\mu A$), as the change in viscosity is only influenced by the absolute change in temperature of the fluid, which is small.

Figure 9d shows the heat flux and HTC. It is observed that the process to de-convolve the discrete time history amplifies measurement noise. The raw heat flux is indicated in grey. A moving average is performed to improve clarity in the trend of the heat flux over the test time. The HTC is calculated using the raw heat flux value and is shown in dark green. The uncertainty on the calculated HTC value is indicated in light green. The calculated HTC shown in Figure 9, uses an estimated value for the fluid temperature, T_{fi}, based on a linear interpolation between inlet and outlet fluid temperature as the extra fluid thermocouple was not yet installed for this test.

Discussion – Air results

The air temperature at the inlet (T_{in}) and outlet (T_{out}) shows a difference after $t = 21.7$ s, approximately 1 s after the trigger valve is opened. This difference indicates that there is heat transferred to the fluid as expected and is attributed to heat transfer between the shaft, fluid, and casing.

A significant fluctuation in HTC is present in Figure 9d at $t = 29.5$ s with large uncertainties. This fluctuation corresponds to when the heat transfer direction between the shaft and fluid switches directions. This is shown in Figure 9b where the fluid temperature is initially "hotter" than the shaft surface, then the cold gas slug enters the test section and cooling starts as indicated by the inlet temperature being lower than that of the shaft surface. As the temperature difference passes zero, the HTC approaches infinity causing these fluctuations. This is followed by a region of steady heat transfer, lasting until $t = 90$ s. Thereafter, HTC is seen to increase steadily, and uncertainties increase again as the temperature difference reduces.

This steady region, between $t = 50$ s and $t = 90$ s in this case, of a given test is used to establish HTC for that operating condition. To find the optimum time period to average the values of interest, it is necessary to locate the time window which has the lowest variation. Then, select the longest period over which to average to give the most accurate measurement. The time period selection process is described in significantly more detail in Chapter 5 of Swann (2020). The mean HTC value for the test displayed in Figure 9, produced in this way, is $1.67 \pm 0.9 \times 10^2$ W/m^2 K.

A notable temperature difference is present in Figure 9a between the fluid and shaft surface at the start of the test ($t = 0$ s) before the trigger valve is opened. As the system inversion assumes the shaft initially has a constant radial temperature distribution, the only requirement for determining heat flux is that shaft temperature is steady and uniform. This is because heat flux is only a function of the change in shaft surface temperature, removing the need for the shaft and fluid to be initially equilibrated. As the shaft thermal conductivity is significantly greater than convective heat transfer to stationary air (i.e. the system has a small Biot number), the effect of the initial temperature difference on the radial temperature distribution is expected to be small.

Results with supercritical carbon dioxide

Figure 10 shows results from a single test using sCO$_2$, at conditions specified in Table 7. Compared to the air experiment shown in Figure 9, the heat transfer rate is much higher, resulting in shorter test times and higher temperature gradients.
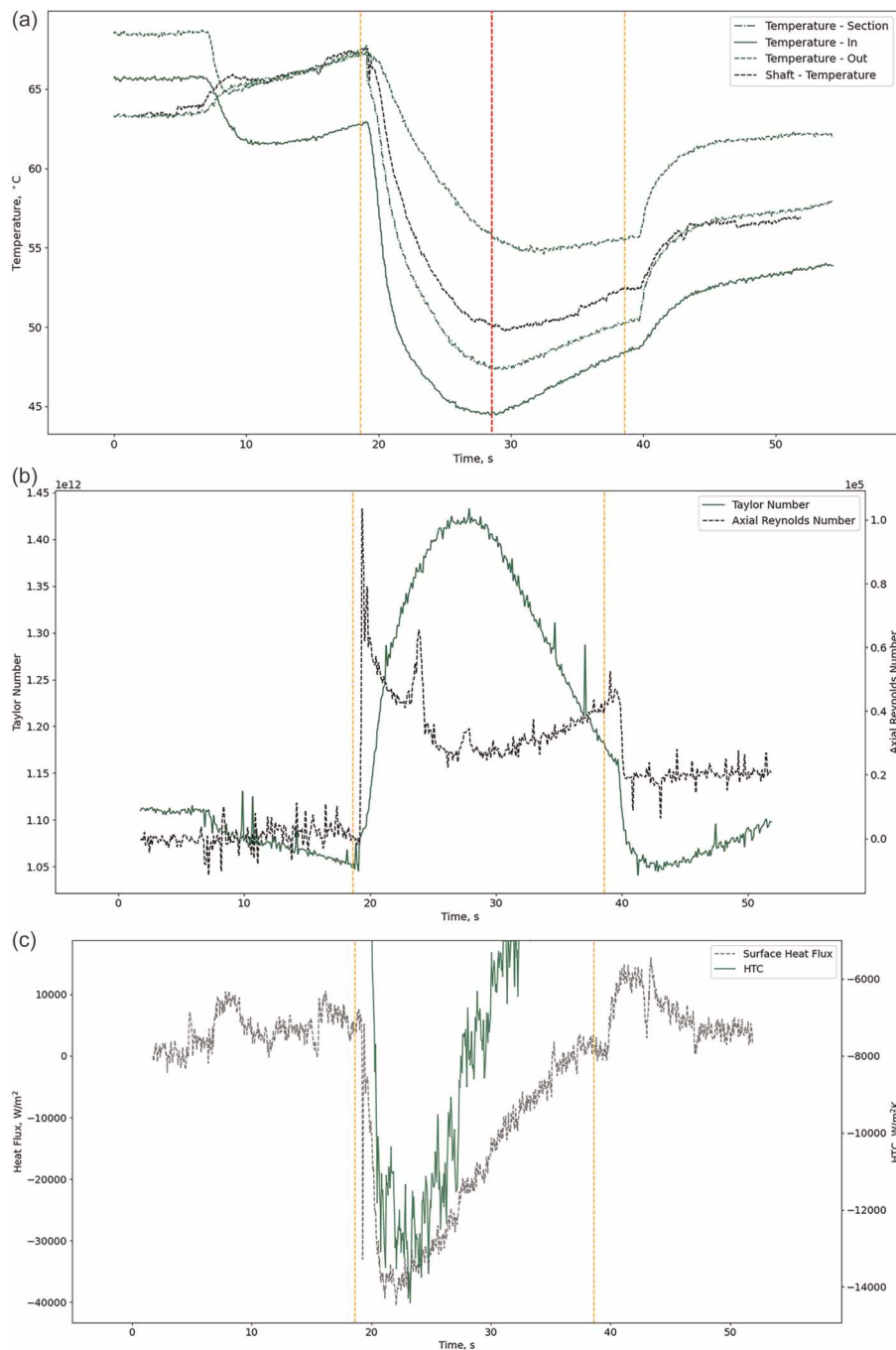
Figure 10. CO_2 Test from top to bottom; (a) temperatures (b) Taylor and axial Reynolds number (c) heat flux and HTC. Yellow vertical dashed lines indicate trigger valve opening and closing. Red dashed line indicates the end of the test time period.

The fluid and shaft temperatures are displayed in Figure 10a. These temperatures show the increased heat transfer with the shaft temperature having a 17.6 degree temperature change over 9.6 s, immediately after the trigger valve is opened indicated by the yellow dashed line. After this high heat transfer region the temperatures begin to rise, indicated by the red dashed line at $t = 28.5$ s. The time period before this, and after the trigger valve is opened, is used as the test time period.

Figure 10b shows the Taylor number and axial Reynolds number reached using the high density sCO$_2$. This shows a maximum Taylor number reached during the sCO$_2$ test of approximately 1.43×10^{12} and a maximum axial Reynolds number of 1.03×10^5. The high Taylor number is the result of the high density and low viscosity of sCO$_2$ compared to the air test condition. This test shows that the HTC measurements of Childs and Turner (1994), whom reached Taylor numbers up to 1.01×10^{11}, can now be expanded upon to include higher Taylor number flows.

Table 7. CO_2 single test nominal settings.

Parameter	Value
Speed (RPM)	30,000
Fluid Inlet Temperature (°C)	50
Fluid Inlet Pressure (MPa)	10
Mass control orifice size (mm)	1.1
Test time (s)	3
Shaft Initial Temperature (°C)	70
Nominal Taylor Number	1×10^{12}
Nominal Axial Reynolds Number	4.0×10^4

To view the change in HTC within the test time window, HTC has been clipped at $-5,000$ W/m^2 K in Figure 10c and traces outside of the test time (i.e. before $t = 19$ s and beyond $t = 39$ s) have been removed, as large fluctuations are present as previously described in the air test condition. In Figure 10c, there is a distinct region where the HTC has stabilised and shows a steady value. This indicates that the test rig operates as expected, showing a short discrete region of low variance over which, the HTC can be averaged to extract an HTC value for this operating condition. This clear region of steady HTC shows that the test rig works well with sCO_2, which is due to its high density, also increasing the achievable Taylor numbers. For this test with an operating Taylor number of $1.32 \pm 0.15 \times 10^{12}$ and axial Reynolds number of $4.45 \pm 0.12 \times 10^4$, the HTC was calculated as $1.17 \pm 0.13 \times 10^4$ W/m^2 K with a Nusselt number of $2.03 \pm 0.24 \times 10^3$ over the time period of 20.05 to 25.9 s.

Discussion – Supercritical carbon dioxide results

There are two critical observations that should be addressed regarding the sCO_2 data. First, Taylor number varies significantly over the time period when HTC value was evaluated, that is, $t = 20.05$ s to $t = 25.9$ s. Taylor number varies between 1.1×10^{12} and 1.4×10^{12}. To evaluate the effect of the change in Taylor number on the HTC, the time period was split into 6 equal segments, each of 0.975 s. For each segment, the average Taylor number and HTC were calculated. Evaluating the change in Taylor number with the change in HTC, the relationship in Equation 16 for dependence of HTC on Taylor number was established. While dependency on other parameters is not covered here (i.e. Re_a), this simple approximation captures the leading term and form of the relationship.

$$\mathrm{Nu} = f(\mathrm{Re}_a, k, D_h) + 10^{-8}\,\mathrm{Ta} \qquad (16)$$

Taking this dependence and evaluating the variation in HTC over the test time due to the change in Taylor number, the variation in HTC is approximately 15%. As this is the largest variation in Taylor number over the series of tests performed, this is a conservative estimate of the variation in HTC throughout a give set of operating conditions.

The second observation is the reduced noise present in the HTC when using sCO_2 over air. Comparing Figure 10c with Figure 9d, there is significantly reduced noise in the reported heat flux and HTC values. Uncertainty in the averaged value is also reduced from $\pm 54\%$ with air to $\pm 11\%$ with CO_2. This is indicative of the test facility operating with high density, high heat transfer fluids, allowing for more accurate measurements to be made. This reduced uncertainty and noise levels validates the test rig design and suitability for heat flux and HTC measurements of T-C-P flow of high pressure and density gases.

Comparison of nusselt correlations – Air results

Figure 11 shows data collected with air using the methodology described in the previous section. Uncertainty bars are displayed using the average uncertainty in Nusselt number over the time span, for which the HTC value was averaged. Tests were performed at four axial Reynolds number settings. The figure shows two distinct groupings: one for $Re_a = 4,500$ and one for $Re_a \leq 4,000$. The data for $Re_a = 4,500$ show a strong dependence of heat transfer rate on effective Reynolds number, whereas for $Re_a \leq 4,000$ heat transfer is independent of effective Reynolds number.

It is well known that flow structures and more turbulent flow regimes affect heat transfer. In purely axial annular flow, the transition to a turbulent flow regime occurs at $Re_a \approx 3,000$. Meanwhile, it is known that rotation tends to stabilise the flow, thus changing when transition occurs. This is consistent with the trend observed in Figure 11, that shows a transition phenomenon occurring between $Re_a > 4,000$ and $Re_a = 4,500$. This leads to the observed increase in heat transfer, implying that a different, lower heat transfer regime exists for operating points at lower axial Reynolds numbers. As the heat transfer rate is strongly dependent on the flow regime, it is also indicative of a change in flow regime.

Figure 12 shows the data and curve fits corresponding to Equations 17 and 18 for the two groupings. The data show that the lower axial Reynolds number case, the heat transfer rate has no dependence on increasing effective Reynolds number. While for $Re_a = 4,500$, an exponential curve fit was chosen as is standard in literature, with the heat transfer rate proportional to $Re_{\text{eff}}^{0.853}$. The correlation is displayed in Equation 18 and has a 95% confidence interval of ± 8.9 on the measured Nusselt number values. Both curves have good agreement with the data, with the lower axial Reynolds number cases having one outlier. The correlation lines pass through the uncertainties of all other points.

$$Nu = 18.43, \ \ Re_a \leq 4,000 \tag{17}$$

$$Nu = 0.01 \, Re_{\text{eff}}^{0.853}, \ \ Re_a \approx 4,500 \begin{cases} 4.6 \times 10^3 < R2e_{\text{eff}} < 9.1 \times 10^4 \\ 7.4 \times 10^6 < Ta < 8.9 \times 10^8 \end{cases} \tag{18}$$

Figure 12 also shows the correlations developed by Jakoby et al. (1998) and Childs and Turner (1994). The correlations from literature are plotted for the Re_{eff} range they were developed over and show significant differences with each other, especially at higher effective Reynolds numbers. The correlation developed in the current study lies within the uncertainty limits of the experimental data collected and within the spread of the prior art correlations. These differences are indicative of the complexity of the T-C-P flow heat transfer process and that the process may be affected by phenomena that are not captured by the two non-dimensional parameters, Nusselt number and effective Reynolds number.

There are several parameters which may explain the difference in measured Nusselt number for this test facility to those in literature. These include, reference temperature, length scale and Prandtl number (heat capacity). Amongst authors, reference temperature has not been uniformed. For T-C flow, it is standard practice to use the
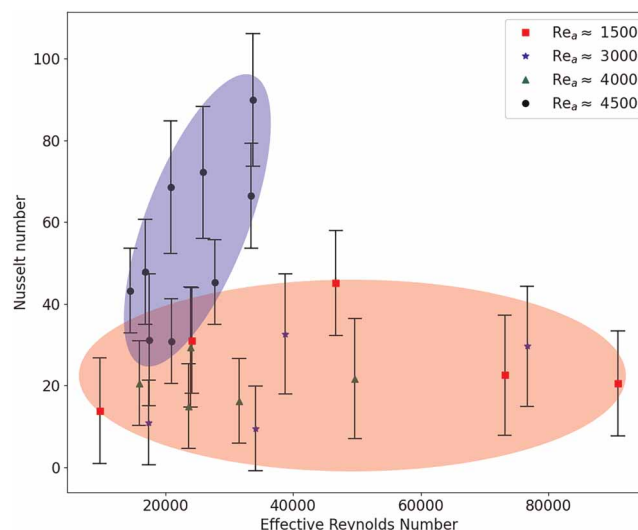

Figure 11. All air data showing averaged Nusselt number against effective Reynolds number.
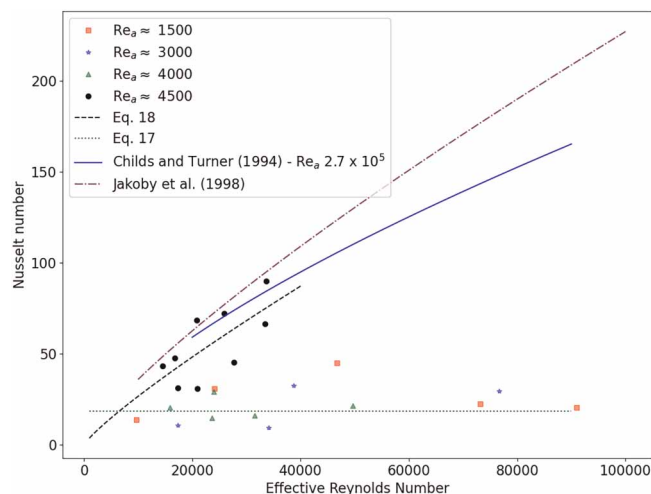
Figure 12. Comparison of Nusselt correlation with literature.

inner and outer wall temperature. However, for T-C-P flow these vary between using inlet and outlet fluid temperature, shaft temperature and outlet temperature, mean (bulk) fluid temperature and shaft temperature. This can alter the scale of the heat transfer coefficient measured.

Another compelling reason for the disparity between literature and these data is the choice of length scale. In T-C flow, the chosen length scale is the hydraulic diameter. This is because development of flow and temperature only occurs in the radial direction. However, for T-C-P flow heat transfer, flow and temperature develop in the axial and radial directions, simultaneously. Within literature, most authors choose the hydraulic diameter to be the length scale for T-C-P flow. This misses the influence of the length ratio (ratio of axial length to gap height) on flow and thermal development as measured by Jakoby et al. (1998). Thus, the difference in geometry used for the different experiments may be the cause for the observed discrepancies.

Conclusions and future work

A test rig design and data analysis methodology for gathering T-C-P heat transfer data with high Taylor number flows is presented. A non-invasive methodology for determining heat flux is demonstrated with an in-depth uncertainty analysis using the Monte-Carlo method.

The full analysis of an example data set operating with air, corresponding to an operating Taylor number of 8.9×10^8 is presented. The high Taylor number capabilities of the rig are established using a supercritical CO_2 test case, demonstrating that test rig, can reach Taylor numbers up to 1.42×10^{12}. Comparison of the HTCs measured for air and CO_2 shows a marked decrease in its uncertainty for CO_2. A systematic analysis of measurement uncertainty in the HTC and data analysis method yield corresponding uncertainty margins of the order ±54% and ±11% for the air and sCO_2 tests, respectively. This shows a positive trend that indicates the rig works effectively when using high density, high heat transfer fluids. To the authors knowledge, this body of work represents the most in-depth analysis of the uncertainty in heat transfer for T-C-P flow regimes.

The collected data using air for Taylor numbers range of 7.4×10^6 to 8.9×10^8 and effective Reynolds number range of 4.6×10^3 to 9.1×10^4, show that there are two distinct flow and heat transfer regimes separated by a critical value of axial Reynolds number. For the current data set, the critical value for axial Reynolds number lies between 4,000 and 4,500. For the data with axial Reynolds number of 4,500, a correlation was created which compares favourably with prior correlations from literature. This shows that the test rig is effective at providing accurate and reliable heat transfer coefficients that are comparable to that of existing literature. Future works will include developing eat transfer correlations at Taylor number ranges near the limit of the test rig, shown in the current study, using supercritical carbon dioxide.

Nomenclature

C Coefficient
D_h Hydraulic diameter (m)
h Convective heat transfer coefficient (W/m^2 K)

I	Impulse matrix
J	Bessel Function of the First Kind
k	Thermal conductivity (W/mK^{-1})
q	Heat flux (W/m^2)
Q	Heat flux matrix
R	Radius (m)
Re	Reynolds number
t	Time (s)
T	Temperature (K)
Ta	Taylor number
V	Velocity (m/s)
α	Thermal diffusivity (k/ρc_p)
λ	Eigen value
ρ	Density (kg/m^3)
ω	Shaft angular speed (rad/s)

Subscripts and Superscripts

a	Axial component
eff	Effective Value
f	Fluid
i	Interval value
inner	Inner value
init	Initial value
n	Eigen function
N	Total number of time intervals
s	Surface
ϕ	Rotational component
0	Zeroth Order
1	First Order

Funding sources

Competing interests

Phillip B. Swann declares that he has no conflict of interest. Ingo H. Jahn declares that he has no conflict of interest. Hugh Russell declares that he has no conflict of interest.

References

Aoki H., Nohira H., and Arai H. (1967). Convective heat transfer in an annulus with an inner rotating cylinder. Bulletin of JSME. 10: 523–532. https://doi.org/10.1299/jsme1958.10.523.

Ball K. S., Farouk B., and Dixit V. C. (1989). An experimental study of heat transfer in a vertical annulus with a rotating inner cylinder. International Journal of Heat and Mass Transfer. 32: 1517–1527. https://doi.org/10.1016/0017-9310(89)90073-2.

Battaglia J.-L., Cois O., Puigsegur L., and Oustaloup A. (2001). Solving an inverse heat conduction problem using a non-integer identified model. International Journal of Heat and Mass Transfer. 44: 2671–2680. https://doi.org/10.1016/S0017-9310(00)00310-0.

Childs P. R. N. and Long C. A. (1996). A review of forced convective heat transfer in stationary and rotating annuli. Proceedings of the Institution of Mechanical Engineers, Part C: Journal of Mechanical Engineering Science. 210: 123–134. https://doi.org/10.1243/PIME_PROC_1996_210_179_02.

Childs P. and Turner A. (1994). Heat transfer on the surface of a cylinder rotating in an annulus at high axial and rotational Reynolds numbers. In Institution of Chemical Engineers Symposium Series. Hemsphere Publishing Corporation, pp. 13–13.

Dawood H. K., Mohammed H. A., Che Sidik N. A., Munisamy K. M., and Wahid M. A. (2015). Forced, natural and mixed-convection heat transfer and fluid flow in annulus: A review. International Communications in Heat and Mass Transfer. 62: 45–57. https://doi.org/10.1016/j.icheatmasstransfer.2015.01.006.

Fénot M., Bertin Y., Dorignac E., and Lalizel G. (2011). A review of heat transfer between concentric rotating cylinders with or without axial flow. International Journal of Thermal Sciences. 50: 1138–1155. https://doi.org/10.1016/j.ijthermalsci.2011.02.013.

Gardarein J.-L., Battaglia J.-L., and Löhle S. (2009). Heat flux sensor calibration using noninteger system identification: Theory, experiment, and error analysis. Review of Scientific Instruments. 80: 025103. https://doi.org/10.1063/1.3079328.

Heshmat H., Walton J. F., and Córdova J. L. (2018). Technology Readiness of 5th and 6th Generation Compliant Foil Bearing for 10 MWE S-CO2 Turbomachinery Systems. In: *6th International Supercritical CO2 Power Cycles Synposium*, Pittsburgh, PA, USA.

Howey D. A., Childs P. R. N., and Holmes A. S. (2012). Air-gap convection in rotating electrical machines. IEEE Transactions on Industrial Electronics. 59: 1367–1375. https://doi.org/10.1109/TIE.2010.2100337.

Jakoby R., Kim S., and Wittig S. (1998). Correlations of the convective heat transfer in annular channels with rotating inner cylinder, volume 4: Heat transfer; electric power; industrial and cogeneration. In Presented at the ASME 1998 International Gas Turbine and Aeroengine Congress and Exhibition, ASME, Stockholm, Sweden, p. V004T09A016. https://doi.org/10.1115/98-GT-097.

Keep J. A., Head A. J., and Jahn I. H. (2017). Design of an efficient space constrained diffuser for supercritical CO_2 turbines. Journal of Physics: Conference Series 821: 012026. https://doi.org/10.1088/1742-6596/821/1/012026.

Masuda H., Yoshida S., Horie T., Ohmura N., and Shimoyamada M. (2018). Flow dynamics in Taylor–Couette flow reactor with axial distribution of temperature. AIChE Journal. 64: 1075–1082. https://doi.org/10.1002/aic.15972.

Schultz D. L. and Jones T. V. (1973). Heat-transfer Measurements in Short-duration Hypersonic Facilities. North Atlantic Treaty Organization, Advisory Group for Aerospace Research and Development (AGARDograph). Available at: https://books.google.com.au/books?id=Fv56nQEACAAJ.

Seghir-Ouali S., Saury D., Harmand S., Phillipart O., and Laloy D. (2006). Convective heat transfer inside a rotating cylinder with an axial air flow. International Journal of Thermal Sciences. 45: 1166–1178. https://doi.org/10.1016/j.ijthermalsci.2006.01.017.

Smith G. P. and Townsend A. A. (1982). Turbulent Couette flow between concentric cylinders at large Taylor numbers. Journal of Fluid Mechanics. 123: 187–217.

Swann P. (2020). Investigation into Taylor-Couette-Poiseuille flow heat transfer for supercritical carbon dioxide turbomachinery. PhD Thesis, The University of Queensland. https://doi.org/10.14264/uql.2020.913.

Tachibana F., Fukui S., and Mitsmura H. (1960). Heat transfer in an annulus with an inner rotating cylinder. Bulletin of JSME. 3: 119–123. https://doi.org/10.1299/jsme1958.3.119.

Yin F., Tiemstra F. S., and Rao A. G. (2018). Development of a flexible turbine cooling prediction tool for preliminary design of gas turbines. The Journal of Engineering for Gas Turbines and Power. 140: 091201. https://doi.org/10.1115/1.4039732.